ACS APPLIED NANO MATERIALS

www.acsanm.org Article

# Nanoscale Ruthenium-Containing Deposits from $Ru(CO)_4I_2$ via Simultaneous Focused Electron Beam-Induced Deposition and Etching in Ultrahigh Vacuum: Mask Repair in Extreme Ultraviolet Lithography and Beyond

Elif Bilgilisoy, Jo-Chi Yu, Christian Preischl, Lisa McElwee-White, Hans-Peter Steinrück,*
and Hubertus Marbach*

**Cite This:** *ACS Appl. Nano Mater.* 2022, 5, 3855−3865

Read Online

ACCESS | Metrics & More | Article Recommendations | Supporting Information

Downloaded via UNIV OF FLORIDA on March 29, 2022 at 21:36:08 (UTC).
See https://pubs.acs.org/sharingguidelines for options on how to legitimately share published articles.

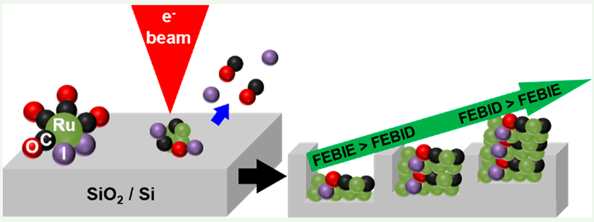

**ABSTRACT:** The deposition of nanoscaled structures with a desired shape on the intended position of the substrate material is crucial for nanomaterial applications. Electron beam-induced deposition with a highly focused beam enables achievement of high accuracy and precision in this respect. Hence, we investigated the focused-electron-beam-induced deposition of Ru-containing deposits on $SiO_2$ and sputter-cleaned silicon in ultrahigh vacuum to achieve comparably clean and morphologically well-defined Ru nanomaterials, which is relevant especially in the field of mask repair for extreme ultraviolet lithography. The precursor $Ru(CO)_4I_2$ was held at 340−345 K, and the applied electron doses were varied from 1.56 to 9.36 C/cm$^2$ using a focused electron beam (5 keV, 1.5 nA, and 10 nm diameter). Local Auger electron spectroscopy along with subsequent sophisticated fitting procedures not only revealed the elemental composition but also enabled determination of the thickness of the fabricated deposits. Ru contents of up to 56% can be achieved at lower electron doses; at higher doses, the Ru content decreases to 45% and simultaneously the content increases. The initially lower I content is attributed to simultaneous focused electron beam-induced etching, which is found to be competing with the deposition process. The etching is evidenced by atomic force microscopy, where the structures are observed to have negative apparent height for low electron doses. With increasing electron doses, the deposits exhibit positive apparent heights because the etching is less pronounced at higher electron doses, once the Ru surface coverage has increased. The high Ru content and difficult balance between electron-induced deposition and etching considerably expand the possibilities of engineering nanostructured materials.

**KEYWORDS:** *focused electron beam-induced deposition (FEBID), ruthenium nanomaterials, focused electron beam-induced etching (FEBIE), scanning electron microscopy (SEM), Auger electron spectroscopy (AES)*

## ■ INTRODUCTION

The controlled fabrication of nanostructured materials on arbitrary substrates remains challenging in industry and academia. Focused electron beam-induced processing (FEBIP), a gas-assisted electron-beam lithography method, is a powerful technique to create such nanoscaled structures.[1−3] In this work, FEBIP includes two different techniques, that is, focused electron beam-induced etching (FEBIE) and focused electron beam-induced deposition (FEBID, also denoted as EBID). FEBIE is the only subtractive variant of FEBIP. Thereby, certain precursor molecules (mostly with halides) are locally decomposed, yielding reactive fragments that are suitable for etching the substrate and forming corresponding volatile compounds with the latter. In this way, FEBIE can effectively etch the substrate material locally. In FEBID, the highly focused electron beam of a scanning electron microscope generally in high vacuum (HV) or, more specifically, in this study in ultrahigh-vacuum (UHV) chamber is used to dissociate adsorbed organometallic precursor molecules. Thereby, the nonvolatile fragments establish a deposit on the substrate, while the volatile dissociation products are pumped out from the vacuum chamber. Consequently, the additive fabrication of metallic or metal-containing deposits can be targeted with organometallic precursor compounds.[4−6]

The FEBIP methods can potentially be applied to fabricate functional structures like tips for scanning probe microscopy,[7] magnetic logic circuits,[8] and single-electron transistors.[9] Furthermore, FEBIP is a state-of-the-art repair method for

**Received:** December 24, 2021
**Accepted:** February 25, 2022
**Published:** March 14, 2022

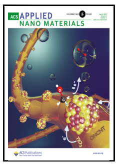

© 2022 American Chemical Society

https://doi.org/10.1021/acsanm.1c04481

photolithography masks in the semiconductor industry.[10,11] Besides the obvious advantages of FEBID, there are several challenges, such as the minimum achievable size of the deposits (e.g., due to proximity effects[12−14]), reproducibility,[1] and material purity.[7,15,16] The material purity is one of the most challenging issues. In order to achieve the highest possible purity, an investigation and understanding of the pathways and kinetics of electron-induced precursor dissociation on a particular substrate is mandatory.[5,17] Gas-phase studies of precursor molecules yield detailed knowledge of the molecule/electron interactions without the influence of the surface. Relevant processes are dissociative electron attachment (DEA) and dissociative ionization (DI).[1,7,18,19] In DEA, the precursor molecule is transformed into an excited anion via the attachment of an electron. This excited anion subsequently dissociates into fragments, often via the release of a single ligand from the precursor. In the DI process, the precursor molecule is ionized by electron impact ionization and the resulting cation dissociates into ions and neutrals. The DI process is mostly linked to the release of multiple ligands, and both DEA and DI represent the primary decomposition and/or deposition of FEBID precursors.[18]

Previous studies reported several suitable vacuum-stable organometallic precursors for FEBID, yielding deposits with metal contents higher than 60 at. %, such as $Fe(CO)_5$,[20−22] $Co(CO)_3NO$,[23] $Co_2(CO)_8$,[24,25] $W(CO)_6$,[26,27] $AgO_2Me_2Bu$,[28] and $AgO_2F_5Prop$.[28] However, the majority of the deposits achieved via FEBID of organometallic precursors require concurrent or postdeposition purification steps. One particularly interesting class of precursors is ruthenium organometallic compounds, which gain more and more importance regarding the manufacturing of electronic chips,[29] the building of interconnect wires,[30] and, most importantly, the repair of extreme ultraviolet lithography masks.[31−33]

There are a few studies addressing Ru-based FEBID processes that report rather low metal contents of the corresponding deposits in the absence of purification steps. A FEBID study with $Ru_3(CO)_{12}$ addresses the growth rate and grain size of the obtained structures but provides no information on the exact content of Ru.[34] In another early study, the ratio of Ru to carbon of a deposit achieved with $EtCp_2Ru$ as the precursor was stated as around 1:9 using energy-dispersive X-ray (EDX) spectra prior to purification. A postdeposition electron-beam irradiation of the structures under an $O_2$ atmosphere was performed as a purification method to remove C impurities, but no quantitative information on the atomic composition of purified Ru structures was provided. However, the thickness of the deposits was reduced by around 76% after the purification process, indicating that C might be “burned off” to some extent.[35] In a very recent study with the same precursor, $EtCp_2Ru$, $H_2O$-assisted purification was performed on FEBID structures on Si, which resulted in a height loss of around 90%. The exact values of the removed impurities [C and O] were difficult to estimate because of the technical limitations of EDX for thin FEBID structures. In a complementary UHV-based surface science study on an adsorbed $EtCp_2Ru$ layer, they found the removal of C to be approximately 60%.[36]

To address the issue of low Ru content of FEBID structures, a recent study used $(\eta^3\text{-}C_3H_5)Ru(CO)_3Br$ as the precursor and applied a gas-assisted purification protocol, that is, annealing the sample in a reducing $H_2/N_2$ gas atmosphere.[37] The Ru content of the as-deposited material was 23 at. % and later increased to 83 at. % after the subsequent purification protocol with $H_2/N_2$. However, this postdeposition treatment has the major drawback of significantly changing the deposit morphology.

A recently published paper reports on gas-phase and surface science studies with $Ru(CO)_4I_2$ and $Ru(CO)_4Br_2$ as precursors.[38] The authors examined electron-induced reactions and performed EBID experiments using a macroscopic electron beam (3 kV and ∼1−2 mm diameter spot size). EDX revealed a Ru/halide (Br or I) ratio of ∼1:2. By comparing the reported EDX results with their gas-phase results, the authors claimed that there is a correlation between the DEA observed in the gas-phase study and the primary electron-induced decomposition of the Ru halide (Br and I) precursors in the nonfocused EBID study. Although these precursors yielded promising results, it has been noted in the literature that nonfocused EBID can give quite different results than FEBID.[39] However, it is still unclear whether this difference is due to different electron-beam parameters or different vacuum conditions.

To prevent unintended effects of purification methods, such as collapse of the deposited structure,[37] an ideal FEBID process would yield pure metallic Ru nanostructures. For certain precursors, such as $Fe(CO)_5$ and $Co(CO)_3NO$, FEBID carried out under UHV conditions indeed can yield clean metallic deposits.[20,23] It has been shown that an autocatalytic growth process takes place in UHV at room temperature, causing the precursor molecules to dissociate on the initial FEBID deposit upon prolonged precursor dosage such that a clean metallic deposit is formed. In this work, we address one of the most promising Ru-based organometallic compounds from the literature, $Ru(CO)_4I_2$, using the impact of a tightly focused electron beam from a scanning electron microscope (SEM) with the aim of fabricating clean Ru nanomaterials in UHV at room temperature without subsequent purification. The quality of the volatile precursor in the gas phase is monitored with quadrupole mass spectrometry. A quantitative analysis regarding changes in chemical composition and thickness of FEBID structures is carried out using Auger electron spectroscopy (AES) and scanning Auger microscopy (SAM). Furthermore, we discuss and compare our results with the previously published gas-phase and nonfocused EBID studies of the same precursor.

## ■ EXPERIMENTAL SECTION

**Synthesis.** $Ru(CO)_4I_2$ was synthesized using a modified literature procedure.[40−42] A solution of $Ru_3(CO)_{12}$ (178.2 mg, 0.2787 mmol, Acros Organics) and hexanes (400 mL) was prepared in a 500 mL Schlenk flask and subsequently purged with hexanes saturated with CO for approximately 10 min. The flask was then irradiated with a blue light emitting diode (450−455 nm and 15 W), while continuing to purge with CO for approximately 20 min until the solution turned clear. The solution was then purged with $N_2$ in order to remove residual CO and thereafter cooled to 233 K using an acetonitrile/dry ice cooling bath. A cooled solution of iodine (246.8 mg, 0.9724 mmol, Scientific) in hexanes (50 mL) was added in one lot to the reaction flask via a syringe, whereupon a yellowish-brown solid immediately precipitated. The solvent was removed under vacuum, leaving a yellow-orange solid, which was sublimed at 338 K and 125 mTorr. Crude yield: 208.7 mg, 53.4%. Yield after sublimation: 170.1 mg, 43.6%. The compound was characterized by comparison to literature data.[40,41] IR (hexanes): 2158 (m), 2105 (vs), 2095 (s), 2066 (s) $cm^{-1}$.

**Handling.** The $Ru(CO)_4I_2$ precursor was kept at 253 K and filled into a stainless-steel precursor storage holder under a $N_2$ atmosphere

**Scheme 1. Representation of the FEBID Process: (a) Irradiation of Adsorbed $Ru(CO)_4I_2$ with a Focused Electron Beam; (b) Dissociation of the Precursor and Desorption of Volatile Species; (c) Final Deposition**

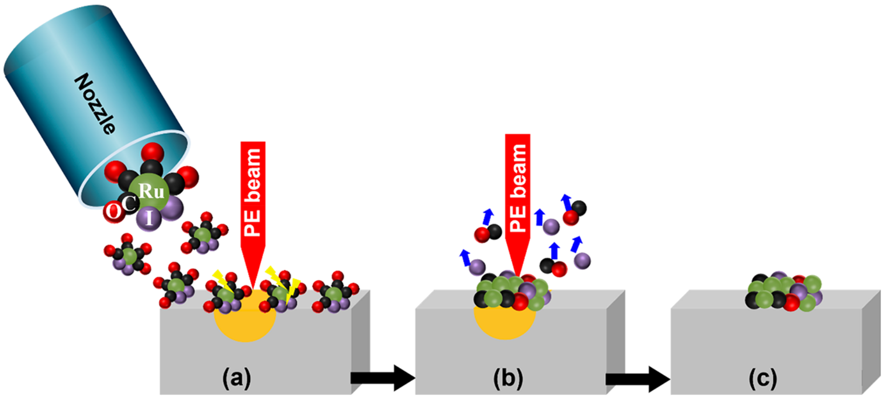

(glovebox). The loaded storage holder was then directly attached to the UHV chamber.

**Deposition.** All structures were fabricated in a modified commercial UHV system (Multiscanlab, Omicron Nanotechnology, Germany) with a base pressure of $p < 2 \times 10^{-10}$ mbar, as depicted in Scheme 1. Electron exposures for SEM and lithography were performed at beam energies of 3 and 5 keV and a beam current of 1.5 nA. The lithography processes were controlled through a custom-developed software based on *LabVIEW 8.6* (National Instruments) and a high-speed DAC PCIe-card (M2i.6021-exp, Spectrum GmbH, Germany).[43] The lithography parameters were a step size of 6.2 nm and a sweep number of 100. The FEBID experiments were carried out on two different substrates, $SiO_2$ (200 nm)/Si(100) and sputtered clean Si.

**Characterization.** Mass spectrometry (MS) was performed using a quadrupole mass spectrometer (Pfeiffer/Prisma QMS 200M) for the gas-phase $Ru(CO)_4I_2$ precursor with a precursor vessel temperature at 340 K. The UHV system consisted of UHV-compatible electron column (Leo Gemini, Zeiss) for SEM (with a nominal resolution better than 3 nm), electron-beam-based lithography (EBL and FEBID), local AES, and SAM (drift-compensated SAM, with a resolution better than 10 nm) using a hemispherical electron energy analyzer (NanoSAM EA U7 analyzer, Omicron). AES analyses were performed using the beam parameters of 15 keV and 3 nA for all results presented in this study, and thus attenuation of the primary electrons by the deposits can be neglected ($\lambda_{AL}$ = 22 nm). SEM images were acquired at a beam energy of 15 keV and a beam current of 400 pA with SmartSEM (Zeiss). Minor contrast and brightness adjustments were applied. The atomic force microscopy (AFM) experiments were performed with a JPK NanoWizard 4 by using the noncontact mode. In Figures 2, 3, and 6, selected representative spectra are shown; for the quantitative analysis, all experiments are used.

The precursor gas was dosed through a nozzle in close proximity to the sample surface. On the basis of simulations using a GIS Simulator (version 1.5),[44] a factor of 30 was estimated for the local pressure increase on the sample surface compared to the chamber background pressure achieved by using the nozzle. For a precursor chamber pressure of $6.0 \times 10^{-8}$ mbar, this corresponds to a local pressure at the surface of about $2.0 \times 10^{-7}$ mbar. The growth regime of the deposits during the FEBID experiments was found in the precursor-limited regime (Section S1).

**Precursor Treatment.** Prior to each FEBID experiment, the precursor was exposed to a vacuum several times via the turbo pump of the UHV chamber to remove residual gases present in the precursor container. During the purification step, the chamber pressure and volatile fragments were observed by ion gauge and MS, respectively. The volatility of the precursor was studied by MS with the precursor container at elevated temperatures. Figure 1 shows the mass spectrum of the $Ru(CO)_4I_2$ precursor at 340 K on a logarithmic scale. The significant peaks are associated with $C^+$ (*m*/*z* 12), $O^+$ (*m*/*z* 16), $CO^+/N_2^+$ (*m*/*z* 28), $Ru^+$ (*m*/*z* 97, 100, 101, 102, 103, and 105), and $I^+$ (*m*/*z* 128 and 129), indicating that at this temperature $Ru(CO)_4I_2$ is volatile enough to be detected by MS.

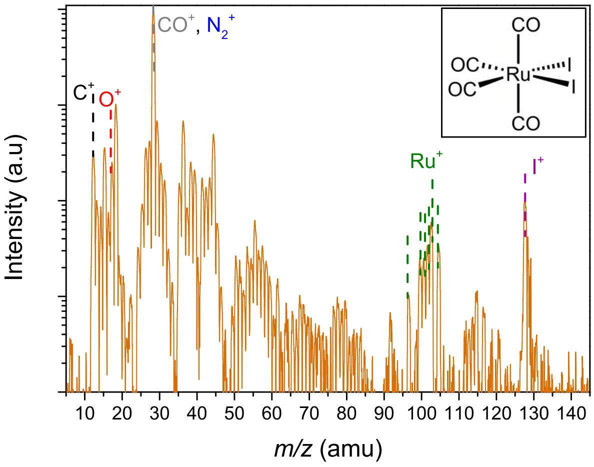

**Figure 1.** Logarithmic plot of the mass spectrum of $Ru(CO)_4I_2$ at a container temperature of 340 K and a precursor pressure of $4 \times 10^{-8}$ mbar.

## RESULTS AND DISCUSSION

**FEBID on $SiO_2$.** In a first step, FEBID experiments were performed on a commercially available $SiO_2$ (200 nm)/Si(100) substrate kept at room temperature. Before FEBID, no specific preparation was applied to clean the $SiO_2$ sample. During the FEBID process, the precursor container was heated to a temperature of about 340−345 K to transfer enough volatile gas into the UHV chamber. Different electron doses were applied to study the deposition behavior of the precursor at a chamber pressure of $6.0 \times 10^{-8}$ mbar (local pressure at the sample = $2.0 \times 10^{-7}$ mbar; see the Experimental Section). The chamber pressure was about 5 times lower compared to the previously mentioned FEBID studies with the $Fe(CO)_5$ and $Co(CO)_3NO$ precursors performed under UHV conditions.[45,46] The comparably low pressures were due to the low vapor pressure of the precursor, and consequently a correspondingly reduced deposition rate was expected. Therefore, a rather low SEM acceleration voltage of 5 keV was selected to increase the secondary electron yield and thus enhance the deposition rate for $Ru(CO)_4I_2$ in the experiments. Using this acceleration voltage, $4 \times 4$ $\mu m^2$ squares were written using a comparably high beam current of 1.5 nA. The

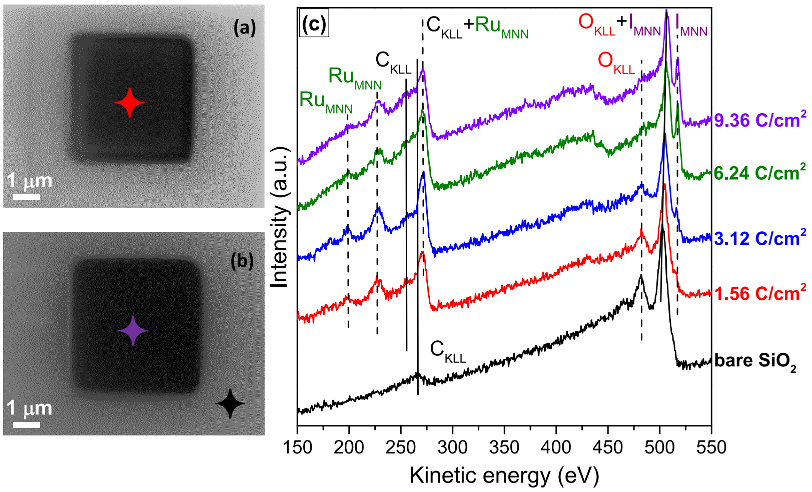

**Figure 2.** SEM images of the FEBID structures produced by an electron dose of 1.56 C/cm$^2$ in (a) and an electron dose of 9.36 C/cm$^2$ in (b) at electron-beam parameters of 5 keV and 1.5 nA. AES spectra from the bare $SiO_2$ surface prior to deposition (black line in (c) and black star on the surface) and the results from FEBID structures prepared using electron doses of up to 9.36 C/cm$^2$. The colored stars in (a) and (b) indicate the positions where the spectra in (c) were acquired.

fabricated FEBID structures were examined with SEM and AES and also partially with AFM.

**SEM and AES on FEBID/$SiO_2$ Deposits.** Parts a and b of Figure 2 depict SEM images of FEBID deposits fabricated with electron exposures of 1.56 and 9.36 C/cm$^2$, respectively. AES spectra acquired on the bare substrate and on deposited structures are plotted in Figure 2c. On the pristine $SiO_2$ surface (black spectrum), only two AES signals are visible. The peak at 265 eV and a weak shoulder at 249 eV are attributed to $C_{KLL}$ Auger transitions of C in carbidic form,[47] and the peaks at 468, 483, and 503 eV are assigned to $O_{KLL}$ Auger transitions of $SiO_2$.[48] After deposition with 1.56 C/cm$^2$, signals at 200, 231, and 273 eV indicative of the $Ru_{MNN}$ transitions[48] are visible, along with the carbidic C signal at 249 eV (the $C_{KLL}$ peak at 265 eV is hidden under the Ru peaks).[47] The characteristic (main) $I_{MNN}$ Auger peaks for I are observed at 509 and 519 eV.[49] While the latter are barely distinguishable for 1.56 C/cm$^2$ (red spectrum in Figure 2c), they are clearly visible at higher doses. The increase of a broad and small peak at approximately 420 eV can also be attributed to I signals because three additional I transitions have previously been reported for the kinetic energy peak positions at 380, 437, and 446 eV.[48]

Because of the overlap of the $Ru_{MNN}$ signals with the $C_{KLL}$ signals and the $I_{MNN}$ signals with the $O_{KLL}$ signals, the AES results were investigated and are presented in Figure 3 on an expanded scale. The spectra were grouped separately for the Ru/C (a) and I/O (b) energy regions. Quantitative analysis of the overlapping Auger peaks is not straightforward, and for a comparison to the literature, different relative sensitivity factors (RSFs) have to be considered when different primary electron-beam energies are used.[47] Auger spectra are often measured (using lock-in techniques), plotted, and analyzed in the differential form, that is, d$I$/d$E$ ($I$ = intensity; $E$ = kinetic energy) versus energy, which makes the separation of overlapping peaks very difficult. Our setup allows for the direct measurement of $I(E)$ with a reasonable signal-to-noise ratio and energy resolution, similar to X-ray photoelectron spectroscopy, which allows for the separation of overlapping peaks by peak fitting. As a reference for the $O_{KLL}$ and $C_{KLL}$ signals, we used the spectrum of the bare $SiO_2$ substrate with its C contamination. A Ru(001) single crystal, cleaned by $Ar^+$ sputtering (Figure S1), served as a reference concerning peak shape, position, and width of the $Ru_{MNN}$ peaks. Its cleanliness was confirmed using a standard procedure, based on the intensity ratio of two peaks in the d$I$/d$E$ spectra at 273 and 231 eV ($I_{273\ eV}/I_{231\ eV}$). We determined this value to be 2.3 after numeric differentiation of our undifferentiated $I(E)$ spectrum (Figure S2). This value agrees very well with literature values from 2.1 to 2.5 for clean Ru(001) surfaces,[48,50] and we can thus use the corresponding spectrum as a reference

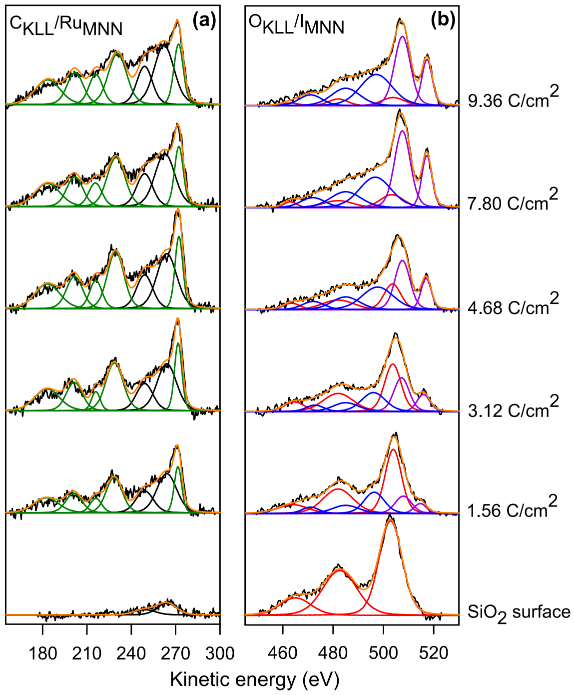

**Figure 3.** AES spectra of FEBID structures for selected electron doses (5 keV and 1.5 nA) after subtraction of a linear BG: (a) $C_{KLL}/Ru_{MNN}$ region; (b) $O_{KLL}/I_{MNN}$ region. Deconvoluted peaks are depicted in green for Ru, black for C, red for surface-related O ($SiO_2$), blue for deposition-related O ($RuO_x$), and light purple for I. The fit envelopes are shown as orange lines and the raw signals as black lines. For details of the fitting procedure, see text.

for fitting the spectra of our FEBID deposits from $Ru(CO)_4I_2$ in Figure 3.

**Quantitative AES on FEBID/$SiO_2$ Deposits.** As the first step in the quantitative analysis, a linear background (BG) was subtracted from the spectra. The AES peaks were fitted with multiple peaks using Voigt functions. For the fitting routines, area constraints were applied for the peaks that belong to one element, i.e., a fixed ratio for the Ru peaks. The resulting signals are plotted in Figure 3 for the $C_{KLL}/Ru_{MNN}$ (a) and $O_{KLL}/I_{MNN}$ (b) regions. In line with the $C_{KLL}$ peak positions from the literature,[47,48] the $C_{KLL}$ region of the bare $SiO_2$ surface in Figure 3a can be fitted with two peaks at 249 and 265 eV (black lines; the orange envelope shows excellent agreement with the data, $R^2 \geq 0.98$). The $Ru_{MNN}$ peaks of the FEBID deposits were fitted based on the peaks of Ru(001) in Figure S2, where five peaks can be clearly identified after the fitting ($R^2 = 0.98$) at 184, 200, 215, 230, and 273 eV. The small peaks of the C impurities are observed at the exact same kinetic energy positions as those for the $SiO_2$ substrate. The characteristic $Ru_{MNN}$ peaks for the FEBID deposits (Figure 3a, green lines) exactly match those found in previous studies.[47,48,51] The $O_{KLL}$ spectrum of the bare $SiO_2$ substrate was fitted by three peaks at 465, 483, and 503 eV (Figure 3b, red lines; $R^2 \geq 0.98$), in good agreement with literature values.[48,52] For the FEBID deposits, the most intense peak was initially found to be at 503 eV, and an additional small peak of 495 eV appeared at lower kinetic energy with increased electron doses. The new peak was assigned to the change from the $SiO_2$ substrate to the O signals related to the precursor dissociation products $RuO_x$. Because the Ru signal was already saturated at the highest dose of 9.36 C/cm$^2$, we assumed that the spectrum was mostly composed of $RuO_x$ signals plus the partly overlapping I signals, both stemming from the formed deposit. We obtained the best fit result with three peaks for the O contribution at 495, 485, and 472 eV (blue) and two peaks for the I contribution at 509 and 519 eV (light purple). The three envelopes of the $SiO_2$-, $RuO_x$- and I-derived peaks were then used to fit the complete data set.

The quantitative analysis of the fitting results of the Ru, C, O and I Auger signals is shown in Figure 4, using the same color code as that in Figure 3 (the C impurity is visible on $SiO_2$, weighted with the attenuation by the deposit, and the surface was subtracted before the quantitative analysis was performed). Overall, we find that the Ru signals exhibit the strongest initial increase, while the I signals initially increase comparably more slowly, with C and O falling in between. The quantitative analysis of the AES data now allows for determination of the composition of the FEBID deposits. Figure 5 depicts the dependence of the atomic concentrations of the different elements for the 4 × 4 $\mu m^2$ FEBID squares deposited with various electron doses. Atomic concentrations were determined from the spectra in Figure 3, considering the AES RSFs derived empirically from standard materials,[48] namely, 0.35 for the $O_{KLL}$ peak at 495 eV and 0.21 for the $I_{MNN}$ peak at 509 eV. For Ru and C, the $Ru_{MNN}$ peak at 231 eV and the $C_{KLL}$ peak at 250 eV were used because these peaks can be best separated from the contributions of other elements.[47,53,54] The corresponding RSFs were calculated separately according to the reference sample standards[48] (Figure S3), yielding 0.18 for the $C_{KLL}$ peak at 250 eV and 0.11 for the $Ru_{MNN}$ peak at 231 eV.

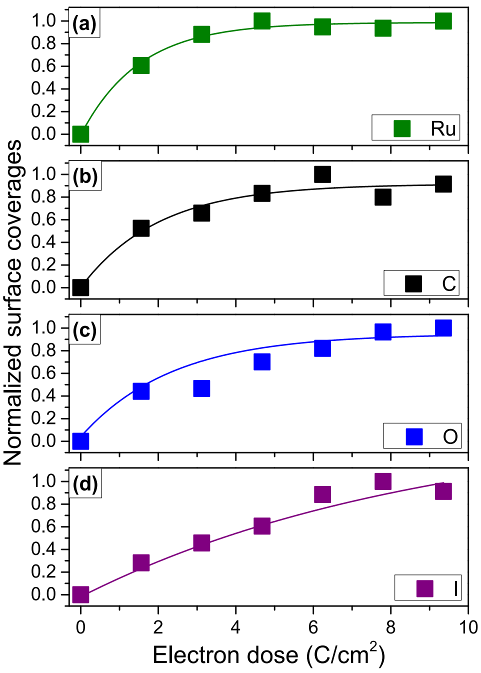

**Figure 4.** Quantitative analysis of the relative amounts of deposited (a) Ru, (b) C, (c) O, and (d) I as a function of the electron dose (C/cm$^2$). The lines in the graph serve as guides to the eye. The signals for each graph are normalized to the signals with the highest intensity.

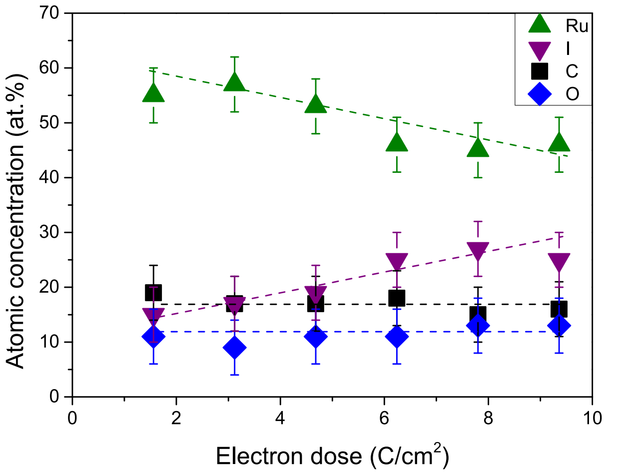

**Figure 5.** Atomic concentrations (at. %) of the elements in deposited structures created from $Ru(CO)_4I_2$ under different electron doses (5 keV and 1.5 nA), as deduced from Figures 3 and 4. The dashed lines drawn in the figure according to the color of each element are guides to the eye. Estimated error bars are denoted in the figure.

The FEBID structures produced with electron doses of 1.56 and 3.12 C/cm$^2$ exhibited compositions with around 56 at. % Ru, 16 at. % I, 18 at. % C and 10 at. % O. Upon an increase in the electron dose up to 7.80 C/cm$^2$, the Ru content decreased by ~11 at. % and the I content increased by ~11 at. %, while the C and O contents did not change significantly. The FEBID structure deposited with the highest electron dose of 9.36 C/cm$^2$ had a composition of around 46 at. % Ru, 25 at. % I, 16 at. % C, and 13 at. % O. From the data shown in Figure 5, it is clear that the highest Ru purities were achieved at low electron doses. We will provide a more detailed analysis on this behavior later in the manuscript.

**Noncontact AFM on FEBID/$SiO_2$ Deposits.** In order to obtain complementary information on the deposition process,

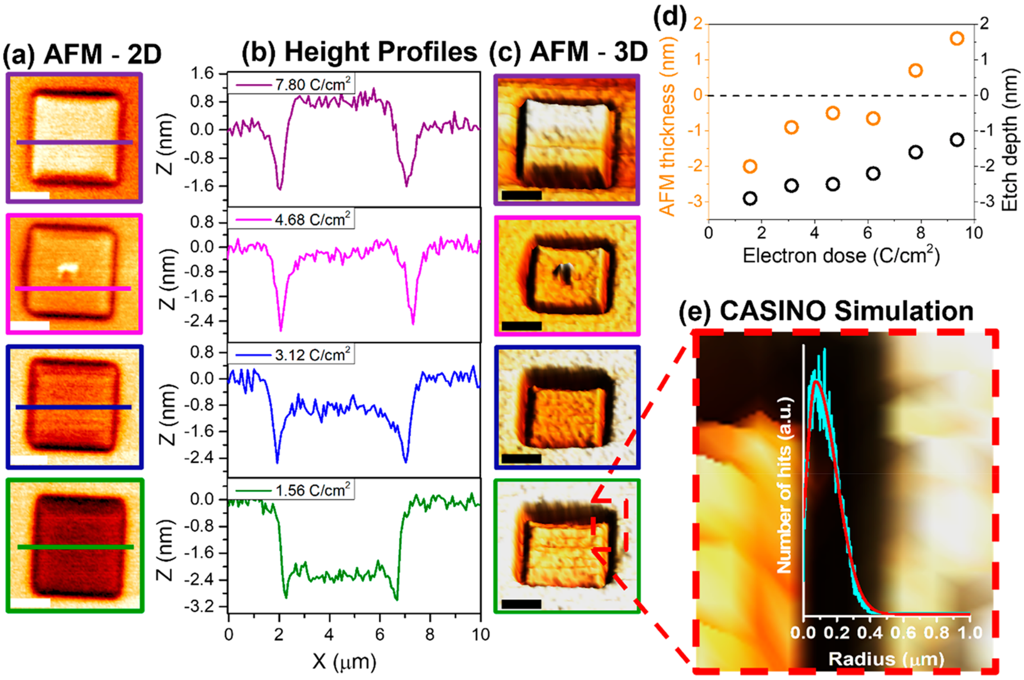

**Figure 6.** (a) 2D AFM images, (b) corresponding line profiles, and (c) 3D AFM images for the FEBID structures produced with electron doses of 1.56 C/cm$^2$ (green lines and frames), 3.12 C/cm$^2$ (blue), 4.68 C/cm$^2$ (pink), and 7.80 C/cm$^2$ (purple). (d) Thickness of the FEBID structures from AFM versus the height of the negative dips. (e) Magnified AFM image superimposed with the simulation of the BSE exit radius (raw data, cyan; fit, red) obtained with the CASINO Monte Carlo program.

we investigated the heights of the FEBID deposits on $SiO_2$ in Figure 2 by noncontact AFM. Parts a−c of Figure 6 depict the 2D AFM images, corresponding height profiles, and 3D AFM images for the FEBID structures for the selected electron doses of 1.56 C/cm$^2$ (green frames and line), 3.12 C/cm$^2$ (blue), 4.68 C/cm$^2$ (pink), and 7.80 C/cm$^2$ (purple), respectively. Notably, the line profiles for the small electron doses in Figure 6b reveal that the deposit is actually lower than the surface level ($Z = 0$ nm) of the substrate. This indicates that initially an etching process occurs along with the deposition process. In Figure 6d, the apparent AFM thickness of the deposit is plotted versus electron dose (orange circles); the data evidence that, up to 6.24 C/cm$^2$, the apparent height is negative and only at high electron doses (≥7.80 C/cm$^2$) is a positive apparent height reached. A detailed analysis of the line profiles in Figure 6b also shows pronounced dips at the edges of the deposits, which are also indicative of etching. The depth of the negative dips is plotted in Figure 6d versus electron dose (open black circles); it changes from −2.8 to −1.3 nm when the electron dose is increased from 1.56 to 9.36 C/cm$^2$.

Similar etching effects, showing up as holes at the edges of deposited structures, were also observed by Mulders et al.[55] when Au(CO)Cl was used as a precursor molecule on $SiO_2$; they were attributed to the secondary electrons generated by backscattered electrons (BSEs). To test this hypothesis, we simulated the radial distribution of BSEs versus number of electrons impinging on the $SiO_2$ substrate with the CASINO Monte Carlo program (version 2.42),[56] using our experimentally applied parameters (5 keV beam with a diameter of 10 nm). The resulting radial distribution was superimposed on top of the enlarged AFM image of Figure 6c (bottom; red-dashed square) in Figure 6e. The width of the etch dip near to the edge of the deposited structure fits very well to the simulated exit radius (~0.4 µm) of BSEs.

Etching of the $SiO_2$ substrate and Ru deposition are competing processes. At low electron doses, etching occurs in the directly irradiated square area and in the BSE exit region (proximity effect area). With increasing dose, Ru deposition in the directly irradiated square seems to occur much faster than that in the BSE exit region (proximity effect area), leading to a decrease of the etching efficiency and a growth of the Ru deposit thickness. This behavior induces the observed etch dips due to continued etching of the regions. The negative thickness of the square deposits deduced from the AFM line scans at low electron doses (Figure 6b,d) demonstrates that etching dominates in this regime and that initially the substrate is etched faster than Ru deposition occurs. The situation changes with increasing electron dose (which we achieve by increasing the dwell time). From these observations, we conclude that the deposited Ru is not etched (from a certain thickness onward) and thus inhibits further etching of the substrate.

Due to the etching effect, the AFM line scans only provide apparent thicknesses (Figure 6b,d). In order to obtain direct and complementary information on the true thickness of the Ru-containing deposits, we measured the attenuation of the Si Auger signal of the underlying substrate as a function of electron dose (these data were not measured for the deposits shown in Figure 2). To be able to directly compare the data, we used electron-beam parameters and electron doses identical with those for the structures on $SiO_2$ shown in Figure 2. The only difference was that we used an oxide-free Si substrate, but we expected no difference in the deposition rate on $SiO_2$ and clean Si.

The clean Si surface was obtained by sputtering the $SiO_2$/Si substrate long enough to completely remove the $SiO_2$ layer (Figure S4), yielding a C- and O-free Si surface. The thicknesses of the deposits were determined from the attenuation of the $Si_{MNN}$ Auger signal of the substrate at a kinetic energy of 1615 eV (Figure S5). Considering the attenuation length for the substrate electrons through the deposited material (Section S2) of $\lambda_{AL}$ = 3.02 nm and an average emission angle $\theta$ of 35°, the layer thickness was calculated according to $I = I_0 \exp[-d/\lambda(E_B) \cos \theta]$. Note that $\lambda_{AL}$ of the $Si_{MNN}$ Auger electrons is much larger than $\lambda_{AL}$ of the $Ru_{MNN}$ Auger electrons (0.57 nm at ~250 eV). Thus, the $Si_{MNN}$ signal is still observed for thicknesses in which the $Ru_{MNN}$ signal has already saturated.

**Comparison of AFM and AES on FEBID/$SiO_2$ Deposits.** In Figure 7a, the deposit thicknesses on clean Si as obtained from the attenuation of the $Si_{MNN}$ Auger (full blue circles) are plotted; they show the expected linear increase of the deposit thickness with electron dose, as depicted with a blue line. Figure 7a also shows the apparent heights of the FEBID structures on $SiO_2$ estimated from AFM line scans (open orange circles; same data as those in Figure 6d) to compare the overall deposition thicknesses and etch depths. The difference between the expected deposit thicknesses and apparent heights can be deduced from the differences of the two data sets in Figure 7a, that is, the difference of the AES and AFM heights. The larger difference at small electron doses (≤3.12 C/cm$^2$) indicates that etching dominates as compared to deposition. As the electron dose is increased, deposition becomes dominant, which is reflected in a positive apparent height. The only decisive factor in the competition between etching and deposition is the variation in electron dose. In Figure 7b, the actual changes between the heights obtained from AES and AFM (Δ = AES − AFM) are plotted in the same graph (black squares; right vertical scale) with the Ru surface coverage from Figure 4a (green squares; left vertical scale). From this figure, it is evident that increasing Ru surface coverage goes along with reduced etching. Therefore, we conclude that Ru mitigates the FEBIE process.

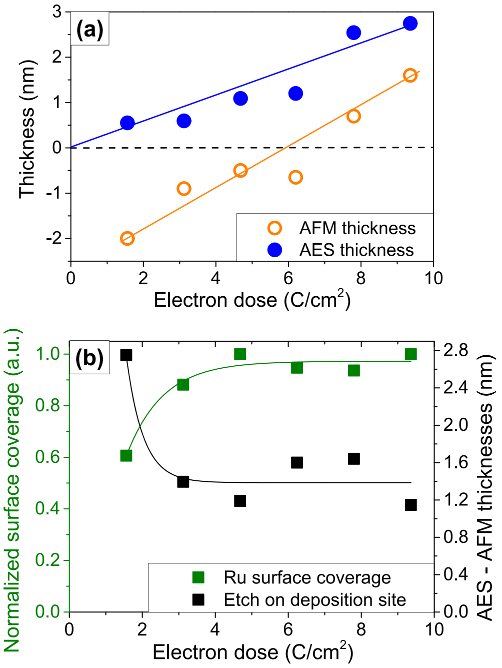

**Figure 7.** (a) Expected thicknesses of the FEBID structures versus electron dose obtained from AES (blue full circles) compared to the apparent thickness obtained from AFM line scans (orange open circles). (b) Difference between expected and apparent heights (black full squares) versus electron dose compared with the Ru surface coverage (green full squares) from Figure 4a. The lines depicted in each graph serve as guides to the eye.

Our results strongly indicate that the FEBIE process is blocked by the FEBID deposits. In previously published papers, FEBIE was extensively studied, and it was proposed that halogen ligands can cause an etching process by forming the volatile byproduct under the influence of an electron beam. While the existing studies mainly focused on $XeF_2$ as the precursor gas on different substrate materials,[57−60] dichloride was also reported to etch a germanium substrate in the presence of an electron beam.[61] The conditions specified in the literature for successful FEBIE correspond to those used in our study, namely, a low hydrocarbon level in the chamber, along with a focused low-energy high-current electron beam, and short or long dwell times depending on the systems.[60,61] Also, in the latter works, the underlying mechanism to trigger FEBIE has been claimed to be the electron-induced decomposition of $SiO_2$ into Si.[3,60] During this process, electron-stimulated desorption of O from the surface creates active sites such as O vacancies.[12,60] Based on the acquired data, the exact mechanism for simultaneous etching/FEBIE and deposition/FEBID must remain speculative. Nevertheless, we propose that I is the etchant, i.e., forms volatile products ($SiI_x$) with surface Si atoms. In this picture, the electron-induced surface activation of $SiO_2$ to SiO* or Si* might promote formation of the latter volatile species. The remaining parts of the precursor molecule, i.e., Ru and carbonyls, are prone to electron-induced deposition, which occurs simultaneously with the etching process. The fact that an increased amount of deposited Ru goes along with a reduced etching rate (cf. Figure 4) leads us to conclude that deposited Ru can deactivate the active sites on the surface and generally blocks access to Si atoms, thus inhibiting further etching. In this regard, the electron dose plays an important role; for higher electron doses, the Ru coverage due to FEBID suppresses the simultaneous etching process. Moreover, the studies combining FEBIE and FEBID typically used two different precursor sources: one for FEBID and one for FEBIE. The advantage of simultaneous FEBID and FEBIE has been reported to be an increased metal content of the deposited material,[62−64] which is also observed in this study for low doses, where etching of the $SiO_2$ substrate dominates. However, also unintended codeposition of etching-related material has been reported.[59,65,66] To overcome this challenge, it appears feasible to use only one precursor source to initiate the competing and simultaneous FEBID and FEBIE processes.

As outlined above, choosing the appropriate experimental conditions is instrumental in obtaining the best compromise between etching and deposition. In our study, we used the halide-ligand-containing $Ru(CO)_4I_2$ precursor and an electron beam with a diameter of ~10 nm, an energy of 5 keV, and a current of 1.5 nA in UHV. Increasing the electron dose by increasing the dwell time also leads to more material deposition in the areas next to the deposit (proximity effect), which, in turn, causes a decrease of the depth of the edge dips (the etching effect). Therefore, the smallest edge dips are expected for the structure produced with the highest electron dose (compare parts a−c of Figure 6).

**FEBID on Si.** As a next step, we will evaluate one more route to increase the thickness of the deposit. The thickness is of high relevance for applications; e.g., it has been shown that a

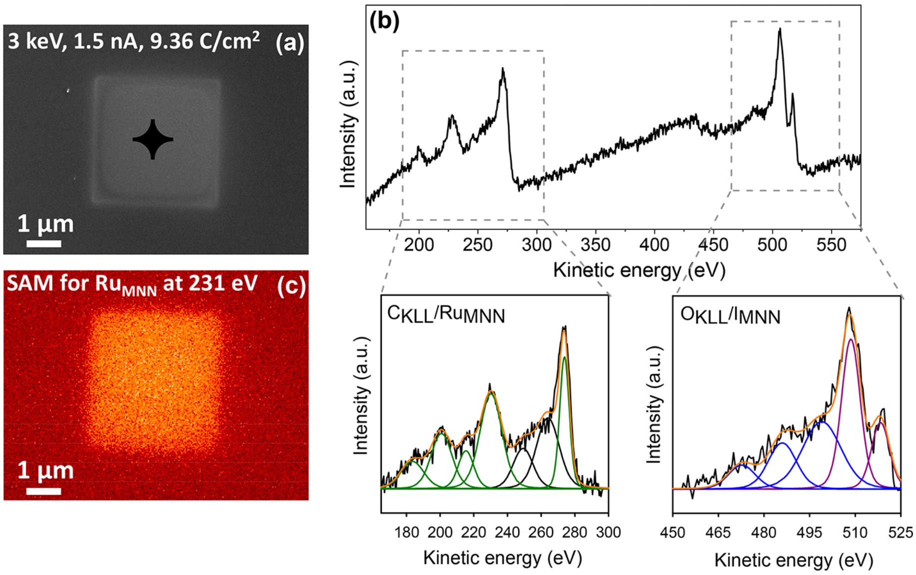

**Figure 8.** (a) SEM image of the FEBID structure under an electron dose of 9.36 C/cm$^2$. The black star represents the point at which spectra were acquired. (b) Local AES spectrum of the deposition from (a) and fitted regions for C$_{KLL}$/Ru$_{MNN}$ and O$_{KLL}$/I$_{MNN}$ depicted with dashed gray lines. (c) SAM image from the FEBID structure for the Ru$_{MNN}$ peak at 231 eV.

2.5 nm thin Ru capping layer is sufficient to protect Mo−Si EUV reflective mirrors.[31] Apart from applying larger electron doses, reducing the step size, or defocusing the beam, one route to increase the growth rate and thus the thickness in FEBID is to decrease the primary electron-beam energy. The main driver for the increased deposition rate is the increase of the secondary electron yield at lower beam energies.[2] Other options include using a nitrogen coflow during FEBID,[35] but this is not applicable to our experimental setup.

As shown in Figures 5 and 6, a good balance between the FEBIE and FEBID processes might yield a high metal content in the structures with sufficient thickness. Lowering the electron-beam energy can increase the contribution of I to the etching process[60] and also increase the thickness of the deposited structure due to the increased secondary electron yield. In this way, it might be possible to establish an optimized balance between etching and deposition rates to obtain high content.

With the goal to increase the thickness of the deposit and the metal concentration, we lowered the primary beam energy from 5 to 3 keV. All other parameters such as the beam current and electron dose were kept constant. In addition, we used a C- and O-free Si surface instead of SiO$_2$. The SEM image of a 4 × 4 $\mu$m$^2$ deposit produced by FEBID on this clean Si substrate using a dose of 9.36 C/cm$^2$ (3 keV, 1.5 nA, and container temperature = 345 K) is depicted in Figure 8a, and the corresponding local Auger spectra are given in Figure 8b. The thicknesses of the deposits obtained with electron-beam energies of 5 and 3 keV were determined from the attenuation of the Si$_{MNN}$ substrate Auger signal at 1615 eV (Figure S6) through the deposited material. For 5 and 3 keV, the Auger signal decreased to 42% and 20% of its original intensity, respectively. From these values, the thicknesses of the layers were calculated as 2−3 and 4−5 nm for 5 and 3 keV, respectively, by considering the previously mentioned attenuation length and average emission angle.

**SEM, AES, and SAM on FEBID/Si Deposits.** To further characterize the deposit and visually demonstrate the selectivity of the FEBID process, we performed SAM at 231 eV. The SAM data in Figure 8c indeed prove the selectivity of FEBID with Ru(CO)$_4$I$_2$ on Si and indicate a significant amount of deposited Ru. To obtain the elemental composition, we also performed local AES on the deposit at the position indicated in Figure 8a. The corresponding spectrum is shown in Figure 8b along with the peak-fitting analysis for the Ru/C and I/O regions (as described above). Quantitative analysis of the structure in Figure 8 yields 52 at. % Ru, 22 at. % I, 14 at. % C, and 12 at. % O. Notably, this Ru content for the 3 keV deposit is, by 6 at. %, larger than the value of 46 at. % for the 5 keV deposit (both for 9.36 C/cm$^2$). To the best of our knowledge, the value of 52 at. % is the highest reported value so far without any pre- and/or postpurification methods applied.

The larger Ru content of the structures in Figure 8 compared to Figure 5 (both for 9.36 C/cm$^2$) goes along with a decrease in the I, O, and C contents by ∼3, ∼1, and ∼2 at. %, respectively, which could be related to the balance between FEBIE and FEBID and also to maintenance of a clean Si surface before deposition.

When our best FEBID results (52 at. % Ru, 22 at. % I, 14 at. % C, and 12 at. % O) are compared to the literature results acquired with a nonfocused electron beam[38] (31 at. % Ru, 56 at. % I, 8 at. % C, and 5 at. % O) using the same precursor molecule under otherwise similar nominal conditions, it is obvious that the lower Ru content (31 vs 52 at. %) of the literature EBID result goes along with the increased concentrations of C, O, and, in particular, I (56 vs 22 at. %). We speculate that the Ru/I ratio is influenced by the electron-beam current density, which is about a factor of 360 larger in our FEBID experiment (300 nA on 20 × 57 $\mu$m$^2$ vs 1.5 nA on ∼15 nm$^2$), and concurrent I-based etching related to this high current density. At the higher electron current density in FEBID than in EBID, deposited species could be subject to additional electron bombardment, thus removing I as etching and desorption products and increasing the metal purity of the deposits.

Finally, we compare the stoichiometry of the deposit with that of the intact precursor Ru(CO)$_4$I$_2$, which is 14 at. % Ru, 29 at. % I, and 57 at. % C and O. In our study, the Ru content of the FEBID deposits is 52 at. %, much higher than that in the precursor. Therefore, we conclude that the tightly focused electron beam leads to the ejection/removal of an average of 3.5 CO ligands and 1.5 I atoms during the balance stages of FEBIE and FEBID. These findings are not much in line with a recently published study comparing gas-phase and surface reactions of the $Ru(CO)_4I_2$ precursor. Therein, the authors showed that the DEA results, on average, in the loss of two CO ligands and the DI in the loss of an average of three CO ligand loss, along with the loss of 0.5 I.[38] Therefore, deposition of the structures from the $Ru(CO)_4I_2$ precursor with a highly focused electron beam in UHV might be explained by the contributions of DI and DEA rather than only DEA. However, it should be noted that the experimental conditions in the gas-phase study are quite different from those used in FEBID and FEBIE. Hence, the comparison between the gas-phase study and the results achieved has to be treated with caution.

## SUMMARY AND CONCLUSION

We prepared Ru-containing deposits on $SiO_2$/Si and sputtered Si substrates by FEBID in UHV using $Ru(CO)_4I_2$ as the precursor. The deposition process was performed at comparably low vapor pressure of $Ru(CO)_4I_2$ in the precursor-limited regime, using a 5 or 3 keV focused electron beam with a current of 1.5 nA and a diameter of 10 nm, at electron doses up to 9.36 $C/cm^2$. The chemical composition and thickness of the deposits were determined using local AES. SAM images provide proof for having a selective deposition process with significant amounts of Ru only deposited in the irradiated region. In addition, we also used AFM to obtain complementary information on the shape and nanoscaled thickness of the deposits. While at this stage the fabricated structures are only nanoscaled in the vertical direction, the presented technique is without a doubt also capable of creating laterally nanostructured materials. Our study reveals that, at low electron doses, FEBIE of the $SiO_2$ substrate by the halide component of the precursor goes along with deposition of a Ru-containing deposit. Because etching dominates in this regime, the deposits show a negative apparent height, as obtained by AFM. At higher doses, that is, when a Ru-containing deposit of a certain thickness has already been formed, the deposit seems to block the etching process and thus to yield an increase in thickness, which consequently yields positive apparent heights. Quantitative analysis of the AES results yields the normalized surface coverages of Ru, I, C, and O as a function of electron dose. Initially higher Ru and lower I contents are attributed to the consumption of I in the etching process, yielding volatile products. For the higher electron doses, we obtain Ru contents of 45−46 at. % at 5 keV and 1.5 nA, which is significantly higher than those reported in the literature so far. This content can be further increased to 52 at. % on the Si substrate by lowering the beam energy to 3 keV, while leaving all other parameters constant.

Our investigations demonstrate that, due to the competition between FEBID and FEBIE at low electron doses, the deposits have a negative apparent height; that is, significant Ru deposition occurs only after a hole has already been etched into the substrate. What on first glance might appear to be a complication might be exploited for new routes to engineer nanostructured materials. One could envisage that FEBIP might be intentionally stopped at the height of the surface level, resulting in a deposit with a high Ru content at the interface of the substrate. Alternatively, a corresponding deposit with negative apparent height could be covered with the substrate material or another material of the right amount using, e.g., FEBID, such that a buried Ru deposit is produced with an overall flat surface. This might open the pathway to a new type of 3D nanostructured material, expanding the applications of buried nanostructures and buried contacts.[67−69] The advantage of the ruthenium carbonyl halide precursor is that it combines the properties for both etching and deposition. Future studies might reveal additional possibilities of tuning the ratio of etching and deposition, expanding the technique even more.

## ASSOCIATED CONTENT

### Supporting Information

The Supporting Information is available free of charge at https://pubs.acs.org/doi/10.1021/acsanm.1c04481.

> AES on a Ru crystal before and after sputtering (Figure S1), AES on a clean Ru crystal with $E \times N(E)$ versus $E$ and $dN/dE$ versus $E$ signal types (Figure S2), AES on clean Ag and Ru substrates with $E \times N(E)$ versus $E$ and $dN/dE$ versus $E$ signal types (Figure S3), AES on the $SiO_2$ substrate before and after sputtering (Figure S4), AES intensities of the $Si_{MNN}$ peak (1615 eV) under different electron doses (Figure S5), AES damping $Si_{MNN}$ signal for clean Si and 5 and 3 keV FEBID structures (Figure S6), calculations for the precursor flux and current density (Section S1), and calculations for the attenuation length, thickness estimation, and information depth (Section S2) (PDF)

## AUTHOR INFORMATION

### Corresponding Authors

**Hans-Peter Steinrück** − *Physikalische Chemie II, Friedrich-Alexander Universität Erlangen-Nürnberg, Erlangen 91058, Germany;* orcid.org/0000-0003-1347-8962; Email: hans-peter.steinrueck@fau.de

**Hubertus Marbach** − *Physikalische Chemie II, Friedrich-Alexander Universität Erlangen-Nürnberg, Erlangen 91058, Germany; Carl Zeiss SMT GmbH, Roßdorf 64380, Germany;* orcid.org/0000-0002-1982-9690; Email: hubertus.marbach@fau.de

### Authors

**Elif Bilgilisoy** − *Physikalische Chemie II, Friedrich-Alexander Universität Erlangen-Nürnberg, Erlangen 91058, Germany;* orcid.org/0000-0002-5295-213X

**Jo-Chi Yu** − *Department of Chemistry, University of Florida, Gainesville, Florida 32611-7200, United States*

**Christian Preischl** − *Physikalische Chemie II, Friedrich-Alexander Universität Erlangen-Nürnberg, Erlangen 91058, Germany*

**Lisa McElwee-White** − *Department of Chemistry, University of Florida, Gainesville, Florida 32611-7200, United States;* orcid.org/0000-0001-5791-5146

Complete contact information is available at: https://pubs.acs.org/10.1021/acsanm.1c04481

### Notes

The authors declare no competing financial interest.

## ■ ACKNOWLEDGMENTS

This work was conducted within the framework of ELENA, a European Union's Horizon 2020 research and innovation program under the Marie Skłodowska-Curie Grant 722149. E.B., C.P., H.-P.S., and H.M. acknowledge financial support by the Deutsche Forschungsgemeinschaft within the research unit FOR 1878/funCOS. L.M.-W. and J.-C.Y. acknowledge the National Science Foundation for support under Grant CHE-1904802.

## ■ REFERENCES

(1) Van Dorp, W.; Hagen, C. W. A Critical Literature Review of Focused Electron Beam Induced Deposition. *J. Appl. Phys.* **2008**, *104*, 081301.

(2) Huth, M.; Porrati, F.; Schwalb, C.; Winhold, M.; Sachser, R.; Dukic, M.; Adams, J.; Fantner, G. Focused Electron Beam Induced Deposition: A Perspective. *Beilstein J. Nanotechnol.* **2012**, *3*, 597−619.

(3) Randolph, S.; Fowlkes, J.; Rack, P. Focused, Nanoscale Electron-Beam-Induced Deposition and Etching. *Crit. Rev. Solid State Mater. Sci.* **2006**, *31*, 55−89.

(4) Carden, W. G.; Lu, H.; Spencer, J. A.; Fairbrother, D. H.; McElwee-White, L. Mechanism-Based Design of Precursors for Focused Electron Beam-Induced Deposition. *MRS Commun.* **2018**, *8*, 343−357.

(5) Yu, J.-C.; Abdel-Rahman, M. K.; Fairbrother, D. H.; McElwee-White, L. Charged Particle-Induced Surface Reactions of Organometallic Complexes as a Guide to Precursor Design for Electron-and Ion-Induced Deposition of Nanostructures. *ACS Appl. Mater. Interfaces* **2021**, *13*, 48333−48348.

(6) Barth, S.; Huth, M.; Jungwirth, F. Precursors for Direct-Write Nanofabrication With Electrons. *J. Mater. Chem. C* **2020**, *8*, 15884−15919.

(7) Utke, I.; Hoffmann, P.; Melngailis, J. Gas-Assisted Focused Electron Beam and Ion Beam Processing and Fabrication. *J. Vac. Sci. Technol., B: Microelectron. Nanometer Struct. Process., Meas., Phenom.* **2008**, *26*, 1197−1276.

(8) Fernández-Pacheco, A.; Serrano-Ramón, L.; Tyliszczak, T.; Chou, K.; Córdoba, R.; Szkudlarek, A.; O'Brien, L.; Kapusta, C.; Ibarra, M.; De Teresa, J. Correlation Between the Magnetic Imaging of Cobalt Nanoconstrictions and Their Magnetoresistance Response. *Nanotechnology* **2012**, *23*, 105703.

(9) Di Prima, G.; Sachser, R.; Trompenaars, P.; Mulders, H.; Huth, M. Direct-Write Single Electron Transistors by Focused Electron Beam Induced Deposition. *Nano Futures* **2019**, *3*, 025001.

(10) Edinger, K.; Becht, H.; Bihr, J.; Boegli, V.; Budach, M.; Hofmann, T.; Koops, H. W.; Kuschnerus, P.; Oster, J.; Spies, P.; Weyrauch, B. Electron-Beam-Based Photomask Repair. *J. Vac. Sci. Technol., B: Microelectron. Nanometer Struct. Process., Meas., Phenom.* **2004**, *22*, 2902−2906.

(11) Liang, T.; Frendberg, E.; Lieberman, B.; Stivers, A. Advanced Photolithographic Mask Repair Using Electron Beams. *J. Vac. Sci. Technol., B: Microelectron. Nanometer Struct. Process., Meas., Phenom.* **2005**, *23*, 3101−3105.

(12) Walz, M.-M.; Vollnhals, F.; Rietzler, F.; Schirmer, M.; Steinrück, H.-P.; Marbach, H. Investigation of Proximity Effects in Electron Microscopy and Lithography. *Appl. Phys. Lett.* **2012**, *100*, 053118.

(13) Plank, H.; Smith, D. A.; Haber, T.; Rack, P. D.; Hofer, F. Fundamental Proximity Effects in Focused Electron Beam Induced Deposition. *ACS Nano* **2012**, *6*, 286−294.

(14) Drost, M.; Tu, F.; Berger, L.; Preischl, C.; Zhou, W.; Gliemann, H.; Wöll, C.; Marbach, H. Surface-Anchored Metal−Organic Frameworks as Versatile Resists for Gas-Assisted E-Beam Lithography: Fabrication of Sub-10 Nanometer Structures. *ACS Nano* **2018**, *12*, 3825−3835.

(15) van Dorp, W. Sub-10 nm Writing: Focused Electron Beam-Induced Deposition in Perspective. *Appl. Phys. A: Mater. Sci. Process.* **2014**, *117*, 1615−1622.

(16) Huth, M.; Porrati, F.; Dobrovolskiy, O. V. Focused Electron Beam Induced Deposition Meets Materials Science. *Microelectron. Eng.* **2018**, *185*, 9−28.

(17) Spencer, J. A.; Rosenberg, S. G.; Barclay, M.; Wu, Y.-C.; McElwee-White, L.; Howard Fairbrother, D. Understanding the Electron-Stimulated Surface Reactions of Organometallic Complexes to Enable Design of Precursors for Electron Beam-Induced Deposition. *Appl. Phys. A: Mater. Sci. Process.* **2014**, *117*, 1631−1644.

(18) Thorman, R. M.; Kumar, T. P. R.; Fairbrother, D. H.; Ingólfsson, O. The Role of Low-Energy Electrons in Focused Electron Beam Induced Deposition: Four Case Studies of Representative Precursors. *Beilstein J. Nanotechnol.* **2015**, *6*, 1904−1926.

(19) Böhler, E.; Warneke, J.; Swiderek, P. Control of Chemical Reactions and Synthesis by Low-Energy Electrons. *Chem. Soc. Rev.* **2013**, *42*, 9219−9231.

(20) Lukasczyk, T.; Schirmer, M.; Steinrück, H. P.; Marbach, H. Electron-Beam-Induced Deposition in Ultrahigh Vacuum: Lithographic Fabrication of Clean Iron Nanostructures. *Small* **2008**, *4*, 841−846.

(21) Shimojo, M.; Takeguchi, M.; Tanaka, M.; Mitsuishi, K.; Furuya, K. Electron Beam-Induced Deposition Using Iron Carbonyl and The Effects of Heat Treatment on Nanostructure. *Appl. Phys. A: Mater. Sci. Process.* **2004**, *79*, 1869−1872.

(22) Mitsuishi, K.; Liu, Z.; Shimojo, M.; Han, M.; Furuya, K. Dynamic Profile Calculation of Deposition Resolution by High-Energy Electrons in Electron-Beam-Induced Deposition. *Ultramicroscopy* **2005**, *103*, 17−22.

(23) Vollnhals, F.; Drost, M.; Tu, F.; Carrasco, E.; Späth, A.; Fink, R. H.; Steinrück, H.-P.; Marbach, H. Electron-Beam Induced Deposition and Autocatalytic Decomposition of $Co(CO)_3NO$. *Beilstein J. Nanotechnol.* **2014**, *5*, 1175−1185.

(24) De Teresa, J.; Fernández-Pacheco, A.; Córdoba, R.; Serrano-Ramón, L.; Sangiao, S.; Ibarra, M. R. Review of Magnetic Nanostructures Grown by Focused Electron Beam Induced Deposition (FEBID). *J. Phys. D: Appl. Phys.* **2016**, *49*, 243003.

(25) Utke, I.; Michler, J.; Winkler, R.; Plank, H. Mechanical Properties of 3D Nanostructures Obtained by Focused Electron/Ion Beam-Induced Deposition: A Review. *Micromachines* **2020**, *11*, 397.

(26) Koops, H.; Weiel, R.; Kern, D.; Baum, T. High-Resolution Electron-Beam Induced Deposition. *J. Vac. Sci. Technol., B: Microelectron. Process. Phenom.* **1988**, *6*, 477−481.

(27) Wich, T.; Luttermann, T.; Mircea, I. *Computational Methods and Experiments in Materials Characterization III*; Brebbia, C. A., Mammoli, A. A., Eds.; Wit Press, 2007, Vol. *57*, pp 73−82.

(28) Höflich, K.; Jurczyk, J. M.; Madajska, K.; Götz, M.; Berger, L.; Guerra-Nuñez, C.; Haverkamp, C.; Szymanska, I.; Utke, I. Towards The Third Dimension in Direct Electron Beam Writing of Silver. *Beilstein J. Nanotechnol.* **2018**, *9*, 842−849.

(29) Le, V.-G.; Vu, C.-T.; Shih, Y.-J.; Huang, Y.-H. Highly Efficient Recovery of Ruthenium from Integrated Circuit (IC) Manufacturing Wastewater by Al Reduction and Cementation. *RSC Adv.* **2019**, *9*, 25303−25308.

(30) Paolillo, S.; Wan, D.; Lazzarino, F.; Rassoul, N.; Piumi, D.; Tőkei, Z. Direct Metal Etch of Ruthenium for Advanced Interconnect. *J. Vac. Sci. Technol., B: Microelectron. Nanometer Struct. Process., Meas., Phenom.* **2018**, *36*, 03E103.

(31) Yan, P.-y.; Spiller, E.; Mirkarimi, P. Characterization of Ruthenium Thin Films as Capping Layer for Extreme Ultraviolet Lithography Mask Blanks. *J. Vac. Sci. Technol., B: Microelectron. Nanometer Struct. Process., Meas., Phenom.* **2007**, *25*, 1859−1866.

(32) Slaughter, J.; Schulze, D. W.; Hills, C.; Mirone, A.; Stalio, R.; Watts, R.; Tarrio, C.; Lucatorto, T. B.; Krumrey, M.; Mueller, P.; Falco, C. M. Structure and Performance of Si/Mo Multilayer Mirrors for The Extreme Ultraviolet. *J. Appl. Phys.* **1994**, *76*, 2144−2156.

(33) Rosen, R. S.; Viliardos, M. A.; Kassner, M.; Stearns, D. G.; Vernon, S. P. Thermal Stability of Mo/Si Multilayers. *Proceedings of*

*Multilayer Optics for Advanced X-Ray Applications*; International Society for Optics and Photonics, 1992, Vol. *1547*, pp 212−220.

(34) Scheuer, V.; Koops, H.; Tschudi, T. Electron Beam Decomposition of Carbonyls on Silicon. *Microelectron. Eng.* **1986**, *5*, 423−430.

(35) Noh, J.-H.; Stanford, M. G.; Lewis, B. B.; Fowlkes, J. D.; Plank, H.; Rack, P. Nanoscale Electron Beam-Induced Deposition and Purification of Ruthenium for Extreme Ultraviolet Lithography Mask Repair. *Appl. Phys. A: Mater. Sci. Process.* **2014**, *117*, 1705−1713.

(36) Rohdenburg, M.; Winkler, R.; Kuhness, D.; Plank, H.; Swiderek, P. Water-Assisted Process for Purification of Ruthenium Nanomaterial Fabricated by Electron Beam Induced Deposition. *ACS Appl. Nano Mater.* **2020**, *3*, 8352−8364.

(37) Jurczyk, J.; Brewer, C. R.; Hawkins, O. M.; Polyakov, M. N.; Kapusta, C.; McElwee-White, L.; Utke, I. Focused Electron Beam-Induced Deposition and Post-Growth Purification Using the Heteroleptic Ru Complex $(\eta^3\text{-}C_3H_5)Ru(CO)_3Br$. *ACS Appl. Mater. Interfaces* **2019**, *11*, 28164−28171.

(38) Thorman, R.; Jensen, P. A.; Yu, J.-C.; Matsuda, S. J.; McElwee-White, L.; Ingolfsson, O.; Fairbrother, D. H. Electron-Induced Reactions of $Ru(CO)_4I_2$: Gas Phase, Surface, and Electron Beam-Induced Deposition. *J. Phys. Chem. C* **2020**, *124*, 10593−10604.

(39) Mahgoub, A.; Lu, H.; Thorman, R. M.; Preradovic, K.; Jurca, T.; McElwee-White, L.; Fairbrother, H.; Hagen, C. W. Electron Beam-Induced Deposition of Platinum from $Pt(CO)_2Cl_2$ and $Pt(CO)_2Br_2$. *Beilstein J. Nanotechnol.* **2020**, *11*, 1789−1800.

(40) Calderazzo, F.; L'eplattenier, F. Pentacarbonyls of Ruthenium and Osmium. I. Infrared Spectra and Reactivity. *Inorg. Chem.* **1967**, *6*, 1220−1224.

(41) Johnson, B.; Johnston, R.; Lewis, J. Chemistry of Polynuclear Compounds. Part XV. Halogenocarbonylruthenium Compounds. *J. Chem. Soc. A* **1969**, 792−797.

(42) Saha, S.; Captain, B. Synthesis and Structural Characterization of Ruthenium Carbonyl Cluster Complexes Containing Platinum with a Bulky N-Heterocyclic Carbene Ligand. *Inorg. Chem.* **2014**, *53*, 1210−1216.

(43) Vollnhals, F. Exploring Electron Beam Induced Surface Activation for the Fabrication of well-defined Nanostructures: On the Role of Catalytic Processes, Substrates and Precursors. Ph.D. Dissertation, Friedrich-Alexander-Universität Erlangen, Erlangen, Germany, 2015.

(44) Friedli, V.; Utke, I. Optimized Molecule Supply from Nozzle-Based Gas Injection Systems for Focused Electron-and Ion-Beam Induced Deposition and Etching: Simulation and Experiment. *J. Phys. D: Appl. Phys.* **2009**, *42*, 125305.

(45) Schirmer, M.; Walz, M.; Vollnhals, F.; Lukasczyk, T.; Sandmann, A.; Chen, C.; Steinrück, H.; Marbach, H. Electron-Beam-Induced Deposition and Post-Treatment Processes to Locally Generate Clean Titanium Oxide Nanostructures on Si(100). *Nanotechnology* **2011**, *22*, 085301.

(46) Preischl, C.; Le, L. H.; Bilgilisoy, E.; Vollnhals, F.; Gölzhäuser, A.; Marbach, H. Controlled Electron-Induced Fabrication of Metallic Nanostructures on 1 nm Thick Membranes. *Small* **2020**, *16*, 2003947.

(47) Van Staden, M.; Roux, J. The Superposition of Carbon and Ruthenium Auger Spectra. *Appl. Surf. Sci.* **1990**, *44*, 259−262.

(48) Davis, L. E. *Handbook of Auger Electron Spectroscopy*; Physical Electronics Division, 1978.

(49) Krishnan, G. N.; Wood, B. J.; Cubicciotti, D. Auger Electron Spectroscopy Study of The Chemisorption of Iodine on Zirconium. *J. Electrochem. Soc.* **1980**, *127*, 2738.

(50) Zei, M. Epitaxial Growth of Ru and Pt on Pt(111) and Ru(0001), Respectively: A Combined AES and RHEED Study. *J. Nanotechnol.* **2010**, *2010*, 1−12.

(51) Ferrari, P.; Rojas, S.; Diaz-Droguett, D.; Cabrera, A. Evaporation of Low-Vapor Pressure Metals Using a Conventional Mini Electron Beam Evaporator. *Instrum. Sci. Technol.* **2014**, *42*, 142−152.

(52) Nozoye, H.; Matsumoto, Y.; Onishi, T.; Kondow, T.; Tamaru, K. Origin of The Peak Shapes in The Auger Spectrum of Oxygen $(KL_{2,3}L_{2,3})$ on Molybdenum. *J. Phys. C: Solid State Phys.* **1975**, *8*, 4131.

(53) Kanjilal, A.; Catalfano, M.; Harilal, S. S.; Hassanein, A.; Rice, B. Tracking Electron-Induced Carbon Contamination and Cleaning of Ru Surfaces by Auger Electron Spectroscopy. *J. Vac. Sci. Technol., A* **2012**, *30*, 041401.

(54) Kanjilal, A.; Catalfano, M.; Harilal, S.; Hassanein, A.; Rice, B. Time Dependent Changes in Extreme Ultraviolet Reflectivity of Ru Mirrors from Electron-Induced Surface Chemistry. *J. Appl. Phys.* **2012**, *111*, 063518.

(55) Mulders, J.; Veerhoek, J.; Bosch, E.; Trompenaars, P. Fabrication of Pure Gold Nanostructures by Electron Beam Induced Deposition with Au(CO)Cl Precursor: Deposition Characteristics and Primary Beam Scattering Effects. *J. Phys. D: Appl. Phys.* **2012**, *45*, 475301.

(56) Drouin, D.; Couture, A. R.; Joly, D.; Tastet, X.; Aimez, V.; Gauvin, R. CASINO V2. 42—A Fast and Easy-To-Use Modeling Tool for Scanning Electron Microscopy and Microanalysis Users. *Scanning* **2007**, *29*, 92−101.

(57) Martin, A. A.; McCredie, G.; Toth, M. Electron Beam Induced Etching of Carbon. *Appl. Phys. Lett.* **2015**, *107*, 041603.

(58) Randolph, S.; Toth, M.; Cullen, J.; Chandler, C.; Lobo, C. Kinetics of Gas Mediated Electron Beam Induced Etching. *Appl. Phys. Lett.* **2011**, *99*, 213103.

(59) Toth, M.; Lobo, C. J.; Hartigan, G.; Ralph Knowles, W. Electron Flux Controlled Switching Between Electron Beam Induced Etching and Deposition. *J. Appl. Phys.* **2007**, *101*, 054309.

(60) Randolph, S.; Fowlkes, J.; Rack, P. Focused Electron-Beam-Induced Etching of Silicon Dioxide. *J. Appl. Phys.* **2005**, *98*, 034902.

(61) Shawrav, M.; Gökdeniz, Z.; Wanzenboeck, H.; Taus, P.; Mika, J.; Waid, S.; Bertagnolli, E. Chlorine Based Focused Electron Beam Induced Etching: A Novel Way to Pattern Germanium. *Mater. Sci. Semicond. Process.* **2016**, *42*, 170−173.

(62) Shawrav, M. M.; Taus, P.; Wanzenboeck, H. D.; Schinnerl, M.; Stöger-Pollach, M.; Schwarz, S.; Steiger-Thirsfeld, A.; Bertagnolli, E. Highly Conductive and Pure Gold Nanostructures Grown by Electron Beam Induced Deposition. *Sci. Rep.* **2016**, *6*, 1−10.

(63) Perentes, A.; Hoffmann, P. Oxygen Assisted Focused Electron Beam Induced Deposition of Si-Containing Materials: Growth Dynamics. *J. Vac. Sci. Technol., B: Microelectron. Nanometer Struct. Process., Meas., Phenom.* **2007**, *25*, 2233−2238.

(64) Toth, M.; Lobo, C.; Friedli, V.; Szkudlarek, A.; Utke, I. Continuum Models of Focused Electron Beam Induced Processing. *Beilstein J. Nanotechnol.* **2015**, *6*, 1518−1540.

(65) Lobo, C. J.; Martin, A.; Phillips, M. R.; Toth, M. Electron Beam Induced Chemical Dry Etching and Imaging in Gaseous $NH_3$ Environments. *Nanotechnology* **2012**, *23*, 375302.

(66) Toth, M.; Lobo, C. J.; Lysaght, M. J.; Vladár, A. E.; Postek, M. T. Contamination-Free Imaging by Electron Induced Carbon Volatilization in Environmental Scanning Electron Microscopy. *J. Appl. Phys.* **2009**, *106*, 034306.

(67) Jensen, J. A.; Møller, P.; Bruton, T.; Mason, N.; Russell, R.; Hadley, J.; Verhoeven, P.; Matthewson, A. Electrochemical Deposition of Buried Contacts in High-Efficiency Crystalline Silicon Photovoltaic Cells. *J. Electrochem. Soc.* **2003**, *150*, G49.

(68) Ali, R.; Saleem, M. R.; Roussey, M.; Turunen, J.; Honkanen, S. Fabrication of Buried Nanostructures by Atomic Layer Deposition. *Sci. Rep.* **2018**, *8*, 1−10.

(69) Gramse, G.; Kölker, A.; Lim, T.; Stock, T. J.; Solanki, H.; Schofield, S. R.; Brinciotti, E.; Aeppli, G.; Kienberger, F.; Curson, N. J. Nondestructive Imaging of Atomically Thin Nanostructures Buried in Silicon. *Sci. Adv.* **2017**, *3*, e1602586.